Anisotropy of the spectroscopic, optical and thermo-mechanical properties of Li6Eu1-xGdx(BO3)3 crystals optimized for heat-scintillation cryogenic bolometers

Rekia Belhoucif, Matias Velázquez, Yannick Petit, Olivier Plantevin, Marcos A. Couto dos Santos, Frédéric Adamietz, Vincent Rodriguez, Michel Couzi, Olivier Pérez, Oudomsack Viraphong, et al.

Anisotropy of the spectroscopic, optical and thermo-mechanical properties of $Li_6Eu_{1-x}Gd_x(BO_3)_3$ crystals optimized for heat-scintillation cryogenic bolometers

Rekia Belhoucif,[1,2,3] Matias Velázquez,[1,*] Yannick Petit,[1] Olivier Plantevin,[4] Marcos A. Couto dos Santos,[5] Frédéric Adamietz,[6] Vincent Rodriguez,[6] Michel Couzi,[6] Olivier Pérez,[7] Oudomsack Viraphong,[1] Philippe Veber,[1] Dominique Denux,[1] Rodolphe Decourt,[1] and Djamel Ouadjaout[8]

[1] *CNRS, Université de Bordeaux, ICMCB, 87 avenue du Dr. A. Schweitzer, 33608 Pessac cedex, France*
[2] *Faculté de Physique, Laboratoire d'Électronique Quantique, USTHB, BP 32 El alia, 16111 Bab Ezzouar, Alger, Algeria*
[3] *Faculté des Sciences, Département de Physique, UMBB, Boumerdes, Algeria*
[4] *CSNSM UMR 8609, CNRS-Université d'Orsay, Bât. 108, 91405 Orsay Campus, France*
[5] *DFI/CCET/Universidade Federal de Sergipe, 49100-000 São Cristóvão/SE/Brazil*
[6] *ISM, CNRS-Université de Bordeaux, UMR 5255, bâtiment A12, 351 cours de la Libération, 33405 Talence cedex, France*
[7] *CRISMAT, UMR 6508 CNRS/ENSICaen, 6 Bld du Mal Juin, 14050 Caen, France*
[8] *CRTSE Division CCSM, 2 Bld Frantz Fanon, BP 140, Alger-7 Merveilles, Algiers 16038, Algeria*
[*] *matias.velazquez@icmcb-bordeaux.cnrs.fr*

Abstract: Optical, spectroscopic and thermo-mechanical properties of monoclinic $Li_6Eu_{1-x}Gd_x(BO_3)_3$ (x = 0,0.25,0.35) bulk single crystals, grown to be used in the design of heat-scintillation cryogenic bolometers (HSCBs), were investigated. The linear thermal expansion was determined along the a, b, c and c* directions over the temperature range 303–873 K, and its tensor principal coefficients were calculated for both x = 0.25 and x = 0. In addition, the anisotropic thermal conductivity was measured over the temperature range 20-400 K in $Li_6Eu_{0.75}Gd_{0.25}(BO_3)_3$ (LGEB7, x = 0.25), and the principal components of its tensor at 300 K were established. Spectroscopic properties such as polarized absorption, polarized emission, Raman spectroscopy and optical refractive indices are also reported for the first time. Based on the polarized emission spectra, the line and oscillator strengths, the radiative lifetimes and fluorescent branching ratios were obtained. The intensity parameters Ω_λ (λ = 2,4) were obtained and then predicted via the Judd–Ofelt theory. The crystal field parameters and the $^7F_1$ level splitting were discussed using the simple overlap model (SOM) and the method of equivalent nearest neighbours (MENN). The 613 nm emission originates from the $^5D_0 \rightarrow {}^7F_2$ transition and the associated stimulated emission peak cross section reaches its maximum value in π-polarization, $\approx 1.07 \times 10^{-20}$ cm^2 in LGEB7. The thermo-mechanical characterizations and spectroscopic analysis in LGEB7 suggest that this crystal has better optical properties than the Eu^{3+}-doped $Li_6Y(BO_3)_3$ crystals. However, its potential for solid-state laser applications is still quite speculative, unless a clever thermo-mechanical management of the crystal under laser operation is designed.

OCIS codes: (040.6070) Solid state detectors; (120.4530) Optical constants; (140.3380) Laser materials; (140.5680) Rare earth and transition metal solid-state lasers; (160.1190) Anisotropic optical materials; (160.1890) Detector materials; (160.2540) Fluorescent and luminescent materials; (160.4670) Optical materials; (160.4760) Optical properties; (160.5690) Rare-earth-doped materials; (170.6280) Spectroscopy, fluorescence and luminescence; (260.1180) Crystal optics; (260.1440) Birefringence; (260.2510) Fluorescence; (290.3030) Index measurements; (120.7000) Transmission.

#214086 - $15.00 USD Received 16 Jun 2014; revised 23 Jul 2014; accepted 24 Jul 2014; published 11 Sep 2014

References and links

1. M. Martinez, N. Coron, C. Ginestra, J. Gironnet, V. Gressier, J. Leblanc, P. de Marcillac, T. Redon, P. Di Stefano, L. Torres, P. Veber, M. Velazquez, and O. Viraphong, "Scintillating bolometers for fast neutrons spectroscopy in rare events searches," J. Phys. Conf. Ser. **375**(1), 012025 (2012).
2. R. Cattoor, I. Manek-Hönninger, J.-C. Delagnes, B. Bousquet, Y. Petit, V. Jubera, A. Fargues, P. Veber, and M. Velazquez, "Potential of the Eu:LYB crystal as a laser material for DPSS lasers at 613 nm," Proc. SPIE–Int. Soc. Opt. Eng. **8235**, (2012).
3. J. Sablayrolles, V. Jubera, M. Delaigue, I. Manek-Honninger, J.-P. Chaminade, J. Hejtmanek, R. Decourt, and A. Garcia, "Thermal properties and CW-laser operation of the ytterbium-doped borate $Li_6Y(BO_3)_3$," Mater. Chem. Phys. **115**(2-3), 512–515 (2009).
4. M. Chavoutier, V. Jubera, P. Veber, M. Velazquez, O. Viraphong, J. Hejtmanek, R. Decourt, J. Debray, B. Menaert, P. Segonds, F. Adamietz, V. Rodriguez, I. Manek-Honninger, A. Fargues, D. Descamps, and A. Garcia, "Thermal, optical and spectroscopic characterizations of borate laser crystals," J. Sol. St. Chem. **184**(2), 441–446 (2011).
5. C. P. Allier, R. W. Hollander, C. W. E. van Eijk, P. M. Sarro, M. de Boer, J. B. Czirr, J. P. Chaminade, and C. Fouassier, "Thin photodiodes for a neutron scintillator silicon-well detector," IEEE Trans. Nucl. Sci. **48**(41), 1158–1161 (2001).
6. R. D. Peccei and H. R. Quinn, "CP conservation in the presence of pseudoparticles," Phys. Rev. Lett. **38**(25), 1440–1443 (1977).
7. R. Belhoucif, M. Velázquez, Y. Petit, O. Pérez, B. Glorieux, O. Viraphong, P. de Marcillac, N. Coron, L. Torres, E. Véron, A. Kellou, Ph. Veber, R. Decourt, and H. El Hafid, "Growth and spectroscopic properties of ^{6}Li- and ^{10}B-enriched crystals for heat-scintillation cryogenic bolometers used in the rare events searches," CrystEngComm **15**(19), 3785–3792 (2013).
8. L. Gonzalez-Mestres and D. Perret-Gallix, "Neutrinos, dark matter and low temperature detector," Proceedings of the 2nd European Workshop on low temperature devices for the detection of low energy neutrinos and dark matter, Annecy, France, 1–36 (1988) May 2–4.
9. L. Gonzalez-Mestres, "The Ultimate solar neutrino detector: Simultaneous detection of light and phonons in a fast scintillator made of single crystals of an indium compound and cooled to very low temperature," Proceedings of the 2nd International Workshop on Theoretical and Phenomenological Aspects of Underground Physics, Toledo (Spain), september 1991," Nucl. Phys. B Proc. Suppl. **28A**(1), 478–481 (1992).
10. G. Blasse, "The Eu^{3+} luminescence as a measure for chemical bond differences in solids," Chem. Phys. Lett. **20**(6), 573–574 (1973).
11. G. Blasse and A. Bril, "Luminescent properties of $NaGdO_2:Eu^{3+}$," Sol. St. Comm. **4**(8), 373–375 (1966).
12. C. Fu Wen Tian, C. Fouassier, and P. Hagenmuller, "Influence of energy migration on the luminescence in $Li_6Eu(BO_3)_3$, a material with predominant one-dimensional interactions," J. Phys. Chem. Solids **48**(3), 245–248 (1987).
13. N. C. Chang, "Fluorescence and stimulated emission from trivalent europium in yttrium oxide," J. Appl. Phys. **34**(12), 3500–3504 (1963).
14. M. Leskelä and J. Hölsä, "Luminescence properties of Eu^{3+} doped $Li_6Ln(BO_3)_3$ (Ln=Gd,Y) phosphors," Eur. J. Solid State Inorg. Chem. **28**, 151–154 (1991).
15. R. P. Yavetskiy, E. F. Dolzhenkova, M. F. Dubovik, T. I. Korshikova, and A. V. Tolmachev, "Czochralski growth and optical properties of $Li_6Gd_{1-x}Eu_x(BO_3)_3$ (x=0-1) single crystals," J. Cryst. Growth **276**(3-4), 485–490 (2005).
16. Ph. Veber, M. Velazquez, V. Jubera, S. Pechev, and O. Viraphong, "Flux growth of Yb^{3+}-doped RE_2O_3 (RE=Y,Lu) single crystals at half their melting point temperature," CrystEngComm **13**(16), 5220 (2011).
17. C. Chuenarrom, P. Benjakul, and P. Daosodsai, "Effect of indentation load and time on Knoop and Vickers microhardness tests for enamel and dentin," Mater. Res. **12**(4), 473–476 (2009).
18. V. Rodriguez and C. Sourisseau, "General Maker-fringe ellipsometric analysis in multilayer nonlinear and linear anisotropic optical media," J. Opt. Soc. Am. B **19**(11), 2650–2664 (2002).
19. V. Rodriguez, "Quantitative determination of linear and second-harmonic generation optical effective responses of achiral or chiral materials in planar structures: theory and materials," J. Chem. Phys. **128**(6), 064707 (2008).
20. P. Segonds, B. Boulanger, B. Ménaert, J. Zaccaro, J.-P. Salvestrini, M. D. Fontana, R. Moncorgé, F. Porée, G. Gadret, J. Mangin, A. Brenier, G. Boulon, G. Aka, and D. Pelenc, "Optical characterizations of $YCa_4O(BO_3)_3$ and $Nd:YCa_4O(BO_3)_3$ crystals," Opt. Mater. **29**(8), 975–982 (2007).
21. R. S. Krishnan, R. Srinivasan, and S. Devanarayanan, (1979), Thermal expansion of crystals, Pergamon, Oxford.
22. H. Choosuwan, R. Guo, A. S. Bhalla, and U. Balachandran, "Negative thermal expansion behavior in single crystal and ceramic of Nb_2O_5-based compositions," J. Appl. Phys. **91**(8), 5051 (2002).
23. S. P. Biswal, S. O'Connor, and S. R. Bowman, "Thermo-optical parameters measured in potassium-gadolinium-tungstate," CLEO/QWLS 2004, Conference on Lasers and Electro-Optics CLEO'04, San Francisco (CA), USA, May 16–21, paper CThT62, Technical Digest.
24. J. Fan, H. Zhang, J. Wang, Z. Ling, H. Xia, X. Chen, Y. Yu, Q. Lu, and M. Jiang, "Growth, structure and thermal properties of Yb^{3+}-doped $NaGd(WO_4)_2$ crystal," J. Phys. D Appl. Phys. **39**(6), 1034–1041 (2006).
25. J. F. Nye, *Physical Properties of Crystals* (Oxford University Press, 1960).
26. B. J. Skinner, "Physical properties of the end members of the garnet group," Am. Mineral. **41**, 428–436 (1956).

#214086 - $15.00 USD Received 16 Jun 2014; revised 23 Jul 2014; accepted 24 Jul 2014; published 11 Sep 2014

27. W. W. Ge, H. J. Zhang, J. Y. Wang, M. H. Jiang, S. Q. Sun, D. G. Ran, H. R. Xiaa, and R. I. Boughton, "Thermal properties of monoclinic crystal Er^{3+},Yb^{3+}:$Ca_4YO(BO_3)_3$," J. Appl. Cryst. **40**(1), 125–132 (2007).
28. J. Bouvaist and D. Weigel, "Sesquioxyde de plomb, Pb2O3. II. Etude de la dilatation thermique d'un monocristal," Acta Crystallogr. A **26**(5), 510–514 (1970).
29. J. L. Schlenker, G. V. Gibbs, and M. B. Boisen, "Thermal expansion coefficients for monoclinic crystals: a phenomenological approach," Am. Mineral. **60**, 828–833 (1975).
30. S. I. Novikova, "Anisotropy of thermal expansion of solids," Meas. Tech. **27**, 933–938 (1984) (transl. from Izmeritel'naya Tekhnika **10**, 40–42 (1984)).
31. H. Küppers, *International Tables for Crystallography* **Vol. D**, Chapter 1.4, 99–104 (2006).
32. F. Yu, S. Zhang, X. Cheng, X. Duan, T. Ma, and X. Zhao, "Crystal growth, structure and thermal properties of noncentrosymmetric single crystals $PrCa_4O(BO_3)_3$," CrystEngComm **15**(26), 5226–5231 (2013).
33. M. Razegh, *Fundamentals of Solid State Engineering*, 3rd edition (Springer Science, LLC (2009).
34. V. Jubera, Ph. Veber, M. Chavoutier, A. Garcia, F. Adamietz, V. Rodriguez, J.-P. Chaminade, and M. Velazquez, "Crystal growth and optical characterizations of Yb^{3+}-doped $LiGd_6O_5(BO_3)_3$ single crystal: a new promising laser material," CrystEngComm **12**(2), 355–357 (2010).
35. S. D. Ross, "Vibrational assignments in borates with the vaterite structure," J. Mol. Spectrosc. **29**(1-3), 131–145 (1969).
36. G. Barros, E. N. Silva, A. P. Ayala, I. Guedes, C.-K. Loong, J. Wang, X. Hu, and H. Zhang, "Raman spectroscopic characterization of $RECa_4O(BO_3)_3$ (RE=La,Gd) crystals," Vib. Spectrosc. **46**(2), 100–106 (2008).
37. I. C. Hisatsune and N. H. Suarez, "Infrared spectra of metaborate monomer and trimer ions," Inorg. Chem. **3**(2), 168–174 (1964).
38. W. C. Steele and J. C. Decius, "Infrared absorption of lanthanum, scandium, and indium borate and the force constants of borate ion," J. Chem. Phys. **25**(6), 1184–1188 (1956).
39. V. Jubera, J. Sablayrolles, F. Guillen, R. Decourt, M. Couzi, and A. Garcia, "From the infrared to the visible range: spectroscopic studies of ytterbium doped oxyborates," Opt. Commun. **282**(1), 53–59 (2009).
40. M. A. Noginov, H. P. Jenssen, and A. Cassanho, "Periodic absorption in monoclinic crystals," J. Phys. IV Colloque C4, suppl. J. Phys. **4**, 111 (1994).
41. Y. Petit, S. Joly, P. Segonds, and B. Boulanger, "Recent advances in monoclinic crystal optics," Laser and Photonics Reviews **7**(6), 920–937 (2013).
42. O. L. Malta, H. F. Brito, J. F. S. Menezes, F. R. Gonçalves e Silva, S. Alves, Jr., F. S. Farias, Jr., and A. V. M. de Andrade, "Spectroscopic properties of a new light-converting device Eu(thenoytrifluoroacetonate)$_3$2(dibenzyl sulfoxide). A theoretical analysis based on structural data obtained from a sparkle model," J. Lumin. **75**(3), 255–268 (1997).
43. B. M. Walsh, *Advances in Spectroscopy for Lasers and Sensing* (Springer, 2006), 403–433.
44. Lj. Đačanin, S. R. Lukic´, D. M. Petrovic´, M. Nikolic´, and M. D. Dramicanin, "Judd-Ofelt analysis of luminescence emission from Zn_2SiO_4:Eu^{3+} nanoparticles obtained by a polymer-assisted sol-gel method," Phys. B **406**(11), 2319–2322 (2011).
45. W. F. Krupke, "Optical absorption and fluorescence intensities in several rare-earth-doped Y_2O_3 and LaF_3 single crystals," Phys. Rev. **145**(1), 325–337 (1966).
46. P. A. Tanner, in: P. Hänninen, H. Härmä (Eds.), Lanthanide Luminescence in solids, **volume 7** of *Springer Series on Fluorescence* (Springer Berlin Heidelberg, 2011), 183–233.
47. C. Görller-Walrand and K. Binnemans, **volume 23** of *Handbook on the Physics and Chemistry of Rare Earths* (Elsevier, 1996), 121–283.
48. Y. A. R. Oliveira, H. Lima, A. S. Souza, and M. A. Couto dos Santos, "An alternative description for the interaction between the Eu^{3+} ion and its nearest neighbours," Opt. Mater. **36**(3), 655–657 (2014).
49. O. L. Malta, "Theoretical crystal-field parameters for the YOCl:Eu^{3+} system. A simple overlap model," Chem. Phys. Lett. **88**(3), 353–356 (1982).
50. M. A. Couto dos Santos, "Charge factor, symmetry and electrostatics in europium compounds," EPL **87**(6), 67006 (2009).
51. F. Auzel and O. L. Malta, "A scalar crystal field strength parameter for rare-earth ions: meaning and usefulness," J. Phys. (France) **44**(2), 201–206 (1983).
52. J. D. Axe and G. Burns, "Influence of covalency upon rare-earth ligand field splittings," Phys. Rev. **152**(1), 331–340 (1966).
53. P. Porcher, M. Couto Dos Santos, and O. L. Malta, "Relationship between phenomenological crystal field parameters and the crystal structure: The simple overlap model," Phys. Chem. Chem. Phys. **1**(3), 397–405 (1999).
54. P. A. M. Berdowski, M. Buijs, and G. Blasse, "Energy migration in Eu^{3+} compounds; Its dependence on dimensionality and Eu^{3+}-Eu^{3+} distance," J. Phys. Colloque C **7 suppl. n°10, Tome 46**, octobre 1985.
55. M. Inokuti and F. Hirayama, "Influence of energy transfer by the exchange mechanism on donor luminescence," J. Chem. Phys. **43**(6), 1978 (1965).
56. M. Yokota and O. Tanimoto, "Effects of diffusion on energy transfer by resonance," J. Phys. Soc. Jpn. **22**(3), 779–784 (1967).
57. J. M. Hölsä and M. Leskelä, "Optical study of Eu^{3+} luminescence in lithium rare earth borates, $Li_6RE(BO_3)_3$, RE=Gd,Y," J. Lum. **48** & **49**, 497–500 (1991).

#214086 - $15.00 USD Received 16 Jun 2014; revised 23 Jul 2014; accepted 24 Jul 2014; published 11 Sep 2014

58. H. H. Caspers, H. E. Rast, and J. L. Fry, "Optical absorption and fluorescence spectra of EuF_3," J. Chem. Phys. **47**(11), 4505–4514 (1967).

1. Introduction

Because of the threefold (trigonal) or fourfold (tetrahedral) coordination of boron atoms in oxide compounds, borate crystals display a huge variety of structural types, which gives the possibility to select in this family of compounds appropriate materials for chosen applications. Over the past few years, lithium rare earth borates of general formula $Li_6RE(BO_3)_3$:RE' (RE = Y,Gd,Lu; RE' = Ce,Eu,Yb) have attracted considerable attention owing to their potential applications in scintillation detectors or laser cavities [1–5], and their high transparency over a broad spectral range (values up to E_g = 5 eV are encountered). $Li_6Eu_{1-x}Gd_x(BO_3)_3$ single crystals are being developed to be shaped and mounted as the core of heat-scintillation cryogenic bolometers (HSCBs) and in new red/orange laser sources. An emerging frontier research field where these crystals could be successfully employed is the study of solar axions, hypothetical particles providing an elegant solution of the so-called "strong CP problem" of quantum chromodynamics (QCD) [6]. Another major research field where the use of these crystals is currently investigated is the detection and spectroscopy of fast and extremely rare neutrons, which not only helps understanding the ultimate background of the underground sites dedicated to the direct detection of dark matter, but is *per se* a promising research area for environmental issues [1,7]. In all these cases, because of their higher energy resolution and low energy threshold, HSCBs turn out to be very sensitive tools to carry out this exploratory research at the border of today's astroparticle physics. This technology, which has significantly matured since its invention in 1992 [8,9], works at ultralow temperature (≤ 25 mK) and measures an energy release in a single crystal by means of weak heat and light pulses resulting from the same event. This complementarity allows disentangling the nature of the incident particle and consequently to reject the radioactivity background. Indeed, such operation is a mandatory step when the signal rate is vanishingly small. In this work, although the x = 0 composition is addressed, we mainly focused on the x = 0.35 and 0.25 concentrations because they correspond approximately to the maximum of the integrated emission intensity and to the quenching limit, suggesting that these compositions are likely to produce the highest light output [10–12]. In addition, these crystals compositions maintain the presence in large concentrations of ^6Li, ^{10}B and $^{155/157}Gd$ isotopes which possess the highest neutron capture cross section. On the other hand, although $Y_2O_3:Eu^{3+}$ crystals were among the first historical crystals that ever lased [13], Eu^{3+}-based laser operation have not been proved since 1963, which is due to the difficulties in pumping the emitting level with efficient, rugged and compact excitation sources. Recent research on Eu^{3+}-doped $Li_6Y(BO_3)_3$ crystals has suggested that such ions could be efficiently pumped by GaN-based laser diodes [2].

While several investigations have been carried out on $Li_6Eu(BO_3)_3$ and Eu^{3+}:$Li_6Gd(BO_3)_3$ powder samples [12,14,15], to the best of our knowledge, spectroscopic, optical and thermo-mechanical properties of single crystals have not been established In this contribution, the thermo-mechanical, optical and spectroscopic properties of $Li_6Eu_{1-x}Gd_x(BO_3)_3$ bulk crystals have been characterized and discussed, highlighting their anisotropy, in relation with the HSCB or laser operations that can be foreseen. We report for the first time on a detailed study of the polarized emission cross section, JO parameters and radiative lifetime, comparing some of the results with the physical properties of an $Y_{1.866}Eu_{0.134}O_3$ crystal elaborated elsewhere by the flux method [16].

2. Experimental procedures

The $^6Li_6Eu(^{10}BO_3)_3$ (LEB), $Li_6Eu_{0.75}Gd_{0.25}(BO_3)_3$ (LGEB7) and $Li_6Eu_{0.65}Gd_{0.35}(BO_3)_3$ (LGEB6) were first synthesized by conventional solid state reaction and single crystals were grown by a combination of Czochralski and Kyropoulos methods, as explained in [7]. The

#214086 - $15.00 USD Received 16 Jun 2014; revised 23 Jul 2014; accepted 24 Jul 2014; published 11 Sep 2014

^{6}Li- and ^{10}B-enrichment in LEB crystals was performed to improve the detector's response to neutron capture and compare it with non enriched $Li_6Eu(BO_3)_3$ crystals made by other groups in the world. The crystalline phase obtained was characterized by powder X-ray diffraction (XRD) on crushed single crystals. The Gd and Eu contents mapping was determined by means of electron probe microanalysis (EPMA) combined with wavelength dispersion spectroscopy (WDS) analysis. Electron-induced characteristic X-rays were emitted in the region from the surface to a depth of about 2.4 µm, with an electron beam accelerating voltage of 15 keV. The room temperature lattice parameters derived from a Le Bail refinement of the powder XRD pattern with the centrosymmetric space group $P2_1/c$ are a = 7.2358(2) Å, b = 16.5290(4) Å, c = 6.7053(1) Å and β = 105.383(2)° in LGEB7, and a = 7.2359(2) Å, b = 16.5266(4) Å, c = 6.7041(1) Å and β = 105.395(2)° in LGEB6, which leads to Eu densities of 3.9×10^{21} cm^{-3} and 3.4×10^{21} cm^{-3} in LGEB7 and LGEB6 crystals, respectively. Crystallographic orientations were established by the Laue X-ray back reflection method. The crystals were cut by diamond-impregnated metallic blade saw and polished to high flatness. Optical quality could be achieved by means of aluminum-made flat rotating plates polishing. Diamond plates were used as abrasive materials, and an alcohol-based suspension was used as lubricant. Figure 1 shows the types of LGEB6 and LGEB7 crystals shapes that were used for the physical properties measurements, depending on the constraints imposed by the setup. The grown crystals exhibit a good optical quality and a perfect visual transparency. The same kind of crystalline cube was shaped with LGEB7 crystals. For both crystals, parallelepipedic rods were cut along the **a**, **a***, **b**, **c**, **c*** crystallographic axes and the growth direction [4–32].

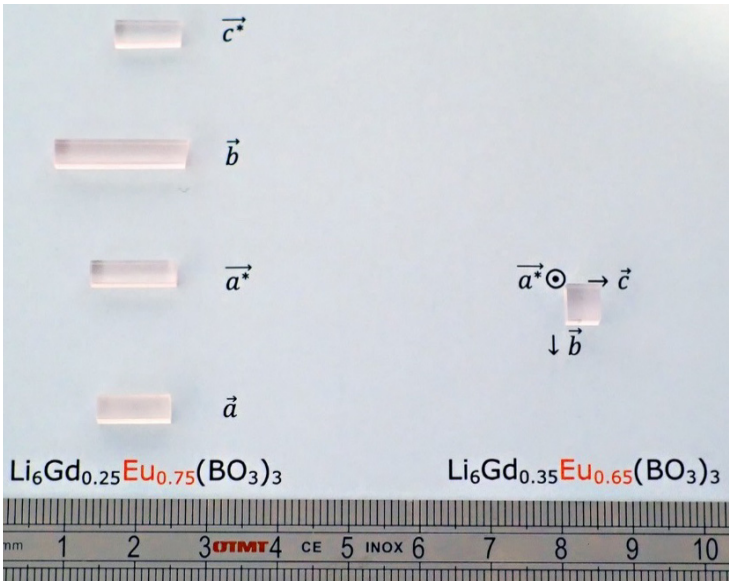

Fig. 1. Shaped LGEB6 and LGEB7 crystals used for the determination of their physical properties.

The composition mapping of LGEB7 single crystals was measured by EPMA (electron probe microanalysis) on a longitudinal section extracted from the core of the bulk at different radial distances. We have determined the Gd depletion equilibrium coefficient in the first stages of the growth according to $k_{Gd} = \frac{x_{Gd,c}}{x_{Gd,l}} \approx 1.12$. Figure 2 shows the Gd concentration as a function of the solidified distance starting from the seed position, in the center of the bulk and at radial distance 2.5 cm. In the inset, the radial profiles are plotted at a solidification distance

#214086 - $15.00 USD Received 16 Jun 2014; revised 23 Jul 2014; accepted 24 Jul 2014; published 11 Sep 2014

just below the first stages of growth and at the bottom of the solidified bulk. These two profiles are virtually the same. The value of the depletion coefficient and the very slightly concave curvature of the profile, are consistent with the expected Gulliver-Scheil type profile for a crystal grown by this normal freezing process. Of course, such features might be explained by the facts that (i) LGB crystals have close but slightly higher melting free energies than LEB crystals, (ii) LGB and LEB crystals lattice energies and standard formation entropies are close, (iii) Gd^{3+} and Eu^{3+} cations have similar molar masses and ionic radii. Nevertheless, at such a concentration level, the role of elastic interactions between Gd^{3+} cations must be significant and Henry's law irrelevant at 0th order. The radial profiles which we measured at different solidified lengths also proved to be uniform. These remarkable axial and radial chemical uniformities of the crystals are outstanding for future HSCBs operation.

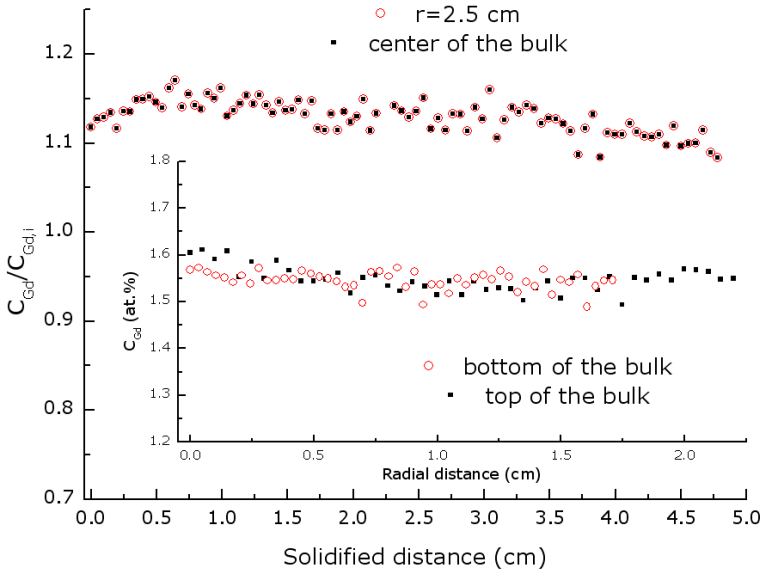

Fig. 2. Gd concentration longitudinal and radial profiles in a LGEB7 single crystal. The x = 0.25 stoichiometry corresponds to 1.31 at. %. The symbol $C_{Gd,i}$ stands for the initial Gd concentration in the melt.

The thermal expansion of the LGEB7 crystals was measured over the temperature range 300–873 K in air using a thermal dilatometer (NETZSCH DIL 402 ED). During the thermal expansion measurements, crystal samples were heated at a constant rate of 2 K min^{-1} from 300 K to 580 K, then from 580 K to 300 K in order to check the reversibility of the thermal cycle. Four rectangular samples were cut from the LGEB7 bulk crystal to determine the thermal expansion ellipsoid, along four different orientations: the three crystallographic axes **a**, **b** and **c***, which define the diagonal components (i = j) and the **c'**-axis cut with the anticlockwise angle $\phi = 40°$ with respect to the **c**-axis, leading to the α_{13} coefficient. Thermal expansion ratio ($\Delta L/L_{RT}$) versus temperature curves were then recorded along **a**, **b**, **a***, **c*** and **c'** crystallographic directions, with L_{RT} the initial length of the sample at room temperature (RT), and ΔL the length variation when temperature changes ΔT. In our experiment, L_{RT}(**a**) = 9.45 mm, L_{RT}(**b**) = 18.30 mm, L_{RT}(**c***) = 13.33 mm, L_{RT}(**a***) = 12.38 mm and L_{RT}(**c'**) = 9.84 mm. The thermal expansion has been measured by dilatometry from RT to 873 K with respect to sapphire, as a reference. The lattice parameters thermal expansion has been obtained by LGEB7 single crystal XRD patterns collected between RT and 950 K, following the experimental procedure described in [7].

The thermal conductivity of LGEB7 crystals was measured directly over the temperature range 20-400 K, and the thermal diffusivity was calculated using the Eq. $D = \kappa/(\rho C_p)$, where ρ

#214086 - $15.00 USD Received 16 Jun 2014; revised 23 Jul 2014; accepted 24 Jul 2014; published 11 Sep 2014

and C_p denote the volumic mass and the heat capacity of the crystal, respectively. Four rectangular bars along **a**, **b**, **c*** and **c'** crystallographic directions with cross section about 3 × 3 mm^2 and length 10 mm (Fig. 1) were mounted in the cryostat and used to study the heat diffusion with silver paste contacts. A small temperature gradient along the sample was realized, and extreme care was taken to eliminate parasitic heat flows between the samples and their surroundings.

The mechanical characterization of the LEB and LGEB7 crystals at room temperature were done by Knoop microhardness by means of a Leica VMHT setup equipped with a diamond square pyramid indenter attached to an incident light microscope. Crystals with flat and smooth (100), (010) and (001) planes, and with growth direction [4–32] and an arbitrary direction were cut from the as-grown LEB and LGEB7 crystals for the static indentation tests, and then mounted on the clamping device to the base of the microscope controlled by an XY travel stage. The selected faces were indented gently by 25 gf (0.245 N) load for a dwell period of 40 s using Knoop indenter. The load is applied in five sample points. The hardness number was defined by the ratio between the indentation load and the area of the residual impression, which depends on the indenter shape [17]. The value of Knoop microhardness HK is calculated using the following expression:

$$HK = 14230\left(F/d^2\right) \tag{1}$$

where F represents the indentation load (g) and d the diagonal of the indentation (μm).

Following the same line of investigation as that already carried out with $^6Li_6Eu(^{10}BO_3)_3$ (LEB) crystals [7], an almost cubic-shaped LGEB7 crystal with dimensions 4.92 mm, 4.81 mm, and 3.96 mm along **c**, **b** and **a*** directions, respectively, was cut and all its surfaces were polished for spectroscopic experiments under polarized light. The polarized absorption spectra from 270 nm to 700 nm corresponding to visible absorption of the Eu^{3+} ions were measured using a Perkin-Elmer spectrometer (Lambda 650). The polarized fluorescence spectra were recorded by means of a spectrophotometer (FLS920, Edinburgh) equipped with a xenon lamp and laser diodes as the excitation sources. Photomultiplier tubes (PMT) (Hamamatsu R928 and R955) were used as detectors in the visible and NIR regions. Fluorescence dynamics of the $^5D_0$-$^7F_2$ transition was investigated as a function of Gd^{3+} cations substitution rates in LGEB6, LGEB7 and LEB single crystals. The experimental lifetimes were determined from the fluorescence decays at room temperature. A selective pulse excitation from an Optic Parametric Oscillator (OPO) emitting a beam with a FWHM pulse duration of 5 ns and with a 10Hz-repetition rate pumped by third harmonic YAG:Nd^{3+} laser was used at 528.3 nm corresponding to the $^5D_1$ excited level. To avoid any spectral overlap between the fluorescence emission and the diffusion of the exciting light, the excited level was selected distinct from the studied level of fluorescence. Moreover, the high excitation level led to a delay time due to multiphonon relaxation. Fluorescence decays were detected by means of a visible photomutiplier (PM) and were recorded with an oscilloscope.

3. Refractive index measurements

In the monoclinic symmetry the principal axes of the optical refractive indicatrix only partially coincide with the crystallographic axes. By symmetry, the crystallographic frame is only connected to the dielectric frame by the C_2 = **b**-axis which is collinear to the *Y*-axis. The other principal axes (*X*-axis and *Z*-axis) lie in the (**a**,**c**)-plane but are rotated with respect to these crystallographic axes. The determination of the rotation angle between these two frames is based on spectroscopic ellipsometry by the extended Brewster angle reflection method at room temperature. The polarized sources used in the measurement were intensity-stable diode lasers at 0.639, 0.785, 0.935, and 1.31 μm, with linear polarization along the p-component in the incident optical plane. These lasers were successively focused on an **a***-, **b**- and **c**-oriented LGEB7 crystal. The rotation of the sample over the wide [-80°,80°] θ-range allows for

#214086 - $15.00 USD Received 16 Jun 2014; revised 23 Jul 2014; accepted 24 Jul 2014; published 11 Sep 2014

collecting the reflected light intensity of the p-polarization component. The setup is totally interfaced and monitored by computer. Data analysis is detailed elsewhere, in [18] and [19]. The relative accuracy of the optical model is not better than ± 5.10^{-3} (case of perfect interfaces). The measured values of n_X, n_Y and n_Z are listed in Table 1. Fitting the data to a simplified Sellmeier dispersion law:

$$n^2 = A + \frac{B}{\lambda^2 + C} + D\lambda^2 \qquad (2)$$

permitted to establish the parameters given in Fig. 3. The parameters corresponding to n_X are not reported because of a fit of insufficient quality.

Table 1. Refractive indices of LGEB7 single crystal at room temperature.

Wavelength (µm)	n_{a^*}	n_b	n_c	n_Z	n_Y	n_X	$\theta(a^*,X)°$
0.639	1.600	1.611	1.624	1.638	1.611	1.586	+ 31
0.785	1.601	1.616	1.615	1.632	1.616	1.584	+ 36
0.935	1.607	1.619	1.609	1.625	1.619	1.591	+ 43
1.31	1.607	1.610	1.594	1.621	1.610	1.580	+ 36

From Table 1, one can deduce that the average maximum birefringence is ≈0.044, which is less than those found, for example, in BBO (~-0.1) and YCOB (≈0.072) crystals [20]. It turns out that there is a change of the sign of the birefringence between 639 nm, where it is slightly positive, and 785 nm, above which it is negative. The peculiar behavior of $n_Y(\lambda)$ is difficult to interpret because the spectral range investigated is far from an absorption band of the crystal. It is likely to be due to the total uncertainty arising from the experimental measurements and the numerical simulation, the latter of which can converge towards very close local minima. Hence, we believe that the θ-variation between 31° and 43° is related to the measurement "scattering" of the refractive index.

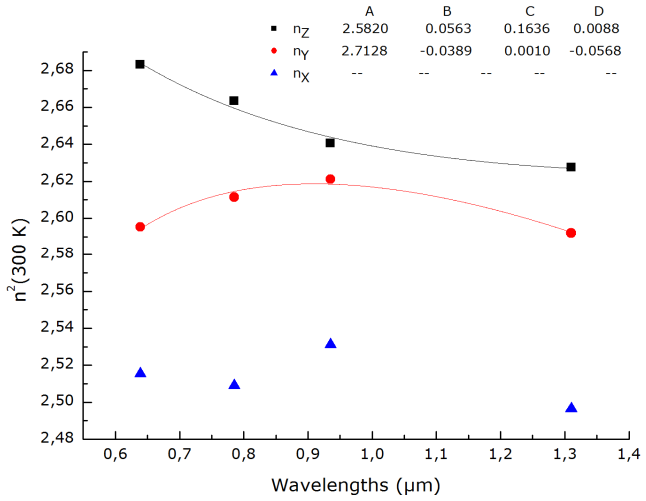

Fig. 3. Coefficients of the Sellmeier Eq. for LGEB7 single crystal.

4. Thermo-mechanical properties

4.1 Thermal expansion

Crystals with low thermal expansion anisotropy and low thermal expansion are desired for both HSCBs (the crystal must fit its mechanical holder at cryogenic temperatures) and laser applications. Thermal expansion is a consequence of the anharmonicity of interatomic potentials forces in solids. As a significant part of the pump power is converted into heat

#214086 - $15.00 USD Received 16 Jun 2014; revised 23 Jul 2014; accepted 24 Jul 2014; published 11 Sep 2014

inside the material and dissipated by its surfaces during laser operation, it is important to determine the linear thermal expansion to estimate its mechanical resistance upon heating by the pump beam. In addition, a lower thermal expansion anisotropy implies *a priori* a more uniform distribution of elastic strain in the optically pumped crystal, hence a lower probability of thermally-induced cracks [21]. Moreover, the thermo–optical coefficients are related to the linear thermal expansion [22]. In this work we present the dilatometry measurements for the LGEB7 crystal. X-ray diffraction on LEB powder samples were used to measure the thermal expansion of the lattice parameters, which was required to complete the thermal expansion profile of the crystal investigated in [7].

It can be seen that the expansion ratio is nearly linear over the whole investigated temperature range. In spite of the fact that there is no phase transition observed in our crystal, a nonlinear behavior is observed from 578 and 700 K especially along the [00-1] and [-100] axes. This behavior may be interpreted in terms of defect structure resulting from thermal strain in this temperature range. On the other hand, the nonlinearity observed below 300 K may be due to the error caused by the thermal dilatometer [23,24]. The average linear thermal expansion coefficient in a given crystallographic directions is defined as:

$$\overline{\alpha} = \frac{1}{L_{RT}} \frac{\Delta L}{\Delta T} \tag{3}$$

The components of the linear thermal expansion tensor, α_{ij}, were evaluated from the slopes of the linear fits related to the linear relationship between $\Delta L / L_{RT}$ and temperature along the considered different crystallographic directions. It is readily established from symmetry considerations [25] that the thermal expansion coefficient tensor for the monoclinic crystal is a symmetrical second rank tensor with four non vanishing components ($\alpha_{11}, \alpha_{22}, \alpha_{33}, \alpha_{13}$) in the orthogonal crystallographic frame (**a**,**b**,**c***). Figure 4 shows the LGEB7 thermal expansion $\Delta L/L_{RT}$ as a function of temperature. Nonlinear least-squares fitting procedures of the thermal expansion data using a parametric Eq. proposed by Skinner [26], have been performed:

$$\Delta L / L_0 = A + BT + CT^2 + DT^{-1} \tag{4}$$

The resulting values in the temperature range 303–750 K are listed in Table 2. The linear thermal expansion coefficients, α, are given by the derivative of Eq. (4).

Table 2. Nonlinear least-squares fitting results of the thermal expansion of a LGEB7 crystal.

LGEB7	A	B	C	D
$\Delta L/L_{RT}$(**a**)	–0,01139	$2{,}85439 \times 10^{-5}$	$-1{,}18442 \times 10^{-8}$	1,18019
$\Delta L/L_{RT}$(**b**)	–0,00386	$1{,}23206 \times 10^{-5}$	$8{,}20172 \times 10^{-9}$	–0,14769
$\Delta L/L_{RT}$(**c'**)	$-4{,}18971 \times 10^{-4}$	$-3{,}61336 \times 10^{-5}$	$2{,}12395 \times 10^{-8}$	–0,11996
$\Delta L/L_{RT}$(**c***)	–0,02354	$6{,}01185 \times 10^{-5}$	$-3{,}53893 \times 10^{-8}$	2,64788
LEB	A	B	C	D
$\Delta L/L_{RT}$(**a**)	0.01302	$-1{,}93601 \times 10^{-5}$	$1{,}94314 \times 10^{-8}$	–2,66632
$\Delta L/L_{RT}$(**b**)	0.00345	$4{,}32658 \times 10^{-6}$	$8{,}79025 \times 10^{-9}$	–1,62561
$\Delta L/L_{RT}$(**c**)	0.00254	$1{,}02222 \times 10^{-5}$	$-1{,}75612 \times 10^{-9}$	–1,6278
$\Delta L/L_{RT}$(**c***)	0.00308	$1{,}24127 \times 10^{-5}$	$-7{,}14878 \times 10^{-9}$	–1,84207

#214086 - $15.00 USD Received 16 Jun 2014; revised 23 Jul 2014; accepted 24 Jul 2014; published 11 Sep 2014

The values of the thermal expansion coefficients along **a**, **b**, **c*** and **c'** are $\alpha_{11} = \alpha_a = 1.20\times10^{-5}\ K^{-1}$, $\alpha_{22} = \alpha_b = 2.04\times10^{-5}\ K^{-1}$, $\alpha_{33} = \alpha_{c^*} = 1.52\times10^{-5}\ K^{-1}$ and $\alpha_{c'} = 1.60\times10^{-5}\ K^{-1}$, respectively. According to the transformation law for second-rank tensor, α_{13} can be deduced from the Eq. given in [27], leading to $\alpha_{31} = \alpha_{13} = -0.26\times10^{-5}\ K^{-1}$. The results show that the thermal expansion coefficients exhibit a substantial dependence with orientation. The thermal expansion decreases according to the sequence $\alpha_b > \alpha_{c^*} > \alpha_a$. The thermal expansion coefficient along the **b**-axis is almost twice that along the **a**-axis. Once α_{13} is known, the thermal expansion can be written as:

$$\alpha_{ij} = \begin{pmatrix} 1.20 & 0 & -0.26 \\ 0 & 2.04 & 0 \\ -0.26 & 0 & 1.52 \end{pmatrix} \times 10^{-5} K^{-1} \quad (5)$$

The diagonalization of this matrix leads to the thermal expansion tensor referred to its principal axes α_I, α_{II}, α_{III}. Neumann's principle dictates that the α_{II} axis coincides with the crystallographic **b**-axis, while the other two principle axes are in the (010)-plane at an angle φ measured counterclockwise from the principal α_{III} axis towards the **c***-axis. The α_{ij} tensor in the principal frame is written as (the details can be found in a previous work [28]):

$$\alpha'_{ij} = \begin{pmatrix} 1.05 & 0 & 0 \\ 0 & 2.04 & 0 \\ 0 & 0 & 1.67 \end{pmatrix} \times 10^{-5} K^{-1} \quad (6)$$

The φ angle can be determined by using the Mohr's circle construction and is evaluated from the following Eq.:

$$\tan 2\varphi = \frac{2|\alpha_{13}|}{\alpha_{33} - \alpha_{11}} = 1.66 \quad (7)$$

The rotation angle φ is 29.5° clockwise from the **c*** direction in the (**a**,**c**)-plane in the LGEB7 crystal, as Fig. 4 right shows.

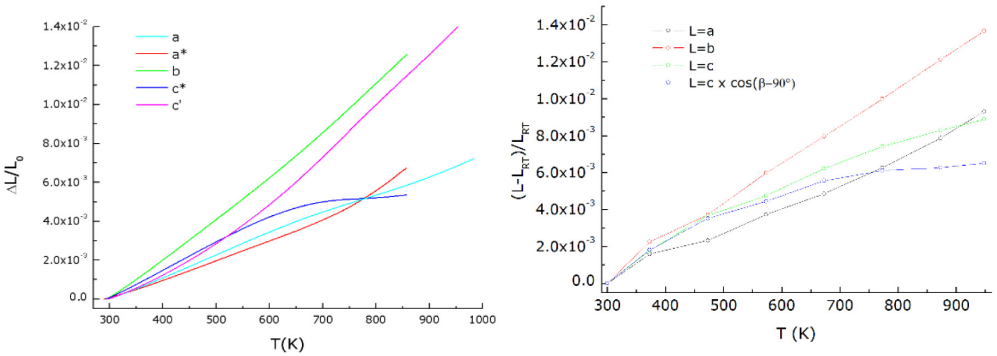

Fig. 4. Left: measured thermal expansion ratio curves of the LGEB7 single crystal as a function of temperature; Right: measured thermal expansion ratio curves of the $^{6}Li_6Eu(^{10}BO_3)_3$ (LEB) single crystal.

We can adopt the formalism based on the unit cell parameters obtained at different temperatures from the LEB single crystal X-ray diffraction characterization [7] (Fig. 4). From these data, α_{ij} can be computed in the same way as explained in relations 3 to 7. The values of the diagonal elements are $\alpha_{11} = \alpha_{\mathbf{a}}$, $\alpha_{22} = \alpha_{\mathbf{b}}$ and $\alpha_{33} = \alpha_{\mathbf{c}^*}$. From the Eq. $\alpha_c = n_i n_j \alpha_{ij}$ [29],

#214086 - $15.00 USD Received 16 Jun 2014; revised 23 Jul 2014; accepted 24 Jul 2014; published 11 Sep 2014

where n_i and n_j are the director cosines of the given direction with the axes of the crystallographic frame, one can deduce $\alpha_{31} = \alpha_{13}$ as the unique unknown quantity of the Eq. once α_c is measured. We obtain:

$$\alpha_{ij} = \begin{pmatrix} 1.14 & 0 & -0.4 \\ 0 & 2.03 & 0 \\ -0.4 & 0 & 1.52 \end{pmatrix} \times 10^{-5} K^{-1} \quad (8)$$

Following the same line of reasoning as before, the α'_{ij} tensor in the principal frame reads:

$$\alpha'_{ij} = \begin{pmatrix} 0.92 & 0 & 0 \\ 0 & 2.03 & 0 \\ 0 & 0 & 1.82 \end{pmatrix} \times 10^{-5} K^{-1} \quad (9)$$

The volume coefficient of thermal expansion, α_V, is given by the (invariant) trace of the linear coefficients [30], as $\alpha_V = \alpha'_{11} + \alpha'_{22} + \alpha'_{33}$, and amounts to 4.76×10^{-5} K^{-1} and 4.77×10^{-5} K^{-1} for LGEB7 and LEB crystals, respectively. Considering the linear thermal expansion of the volume, α_V, and taking into account the relations between thermal expansion and covalence and density of weak bonds [31], one can conclude that the degree of covalence in the chemical bonds of the LGEB7 and LEB compounds is lower than in $PrCa_4O(BO_3)_3$ [32]. In comparison with the maximum anisotropy ratio observed in LEB crystals, $\alpha'_{22}/\alpha'_{11} = 2.2$, the corresponding ratio in the LGEB7 crystal exhibits a lower value, 1.94, which is close to that of $PrCa_4O(BO_3)_3$ [32] and suggests a lower propensity to cleavage in the latter crystals. However, this was not observed experimentally, since both LEB LGEB7 crystals frequently cleaved. The highly anisotropic thermal expansion of the LEB crystals and the overall high values of the thermal expansion coefficients in LEB and LGEB7 crystals might explain why several single crystals were fractured in the process of shaping and polishing before their fabrication in the final form shown in Fig. 1. Such mediocre thermo-mechanical properties clearly question their potential as rugged and efficient solid state optical amplifiers. When temperature increases, atoms begin to move around their equilibrium position, and the more important the anharmonic terms of the interatomic potentials, the higher the thermal expansion. As shown in [7], the distorted gyrobifastigium EuO_8 polyhedra form corrugated chains along the **c** direction. The anisotropy observed is thus quite puzzling because the thermal expansion coefficients in the **a** and **b** directions are lower and higher, respectively, than the one measured along the **c*** direction.

4.2 Thermal conductivity

The thermal conductivity κ of a crystal also stands among the basic properties in the view of HSCB or laser operations. As the LEB and LGEB7 crystals remain electric insulators (electronic and ionic) and do not suffer any sort of long range ordering down to 4 K, only phononic processes should contribute to the thermal conductivity. Figure 5 shows the dependency of the thermal conductivity and diffusivity on temperature. From the measured value of the thermal conductivity at 300 K, and in the same way as detailed in section 4.1, the calculated thermal conductivities along different directions at room temperature are listed in Table 3. The LGEB7 crystal shows a moderate anisotropic thermal conductivity at room temperature, the maximum anisotropy ratio being $\kappa_{II}/\kappa_I = 1.35$. It should also be noted that the conductivity principal axes almost coincide with the crystallographic axes. As the temperature increases, phonon scattering mechanisms become much more effective, the phonon free path gets shorter and the average number of involved phonons is proportional to temperature. Thus, phonon-phonon interactions become increasingly dominant. Since the collision

#214086 - $15.00 USD Received 16 Jun 2014; revised 23 Jul 2014; accepted 24 Jul 2014; published 11 Sep 2014

frequency should be proportional to the number of phonons with which another phonon can collide, the mean free path of phonons are proportional to 1/T at higher temperature. Since, simultaneously, the heat capacity above room temperature varies smoothly, the thermal conductivity can therefore be considered to vary as ~1/T in this regime [33]. The LEB and LGEB7 crystals, as their Y- or Gd-based counterparts, exhibit mediocre thermal conductivities as far as high power laser operations are concerned. Indeed, the higher the thermal conductivity, the higher the damage threshold of the crystal under CW laser operation. The thermal diffusivity of LGEB7 at 300 K is moderately isotropic: 0.78 $mm^2.s^{-1}$ along the **a** direction, 0.82 $mm^2.s^{-1}$ along the **c'** direction, 0.88 $mm^2.s^{-1}$ along the **c*** direction and 1.05 $mm^2.s^{-1}$ along the **b** direction. This latter value is close to that encountered in $Li_6Y(BO_3)_3:Yb^{3+}$ (see Table 4), which leads to an intrinsic cooling time of a typical laser crystal of ≈84 ms, exemplifying the high thermal inertia of such crystals since typical fluorescence lifetimes in these crystals are on the order of 1-2 ms.

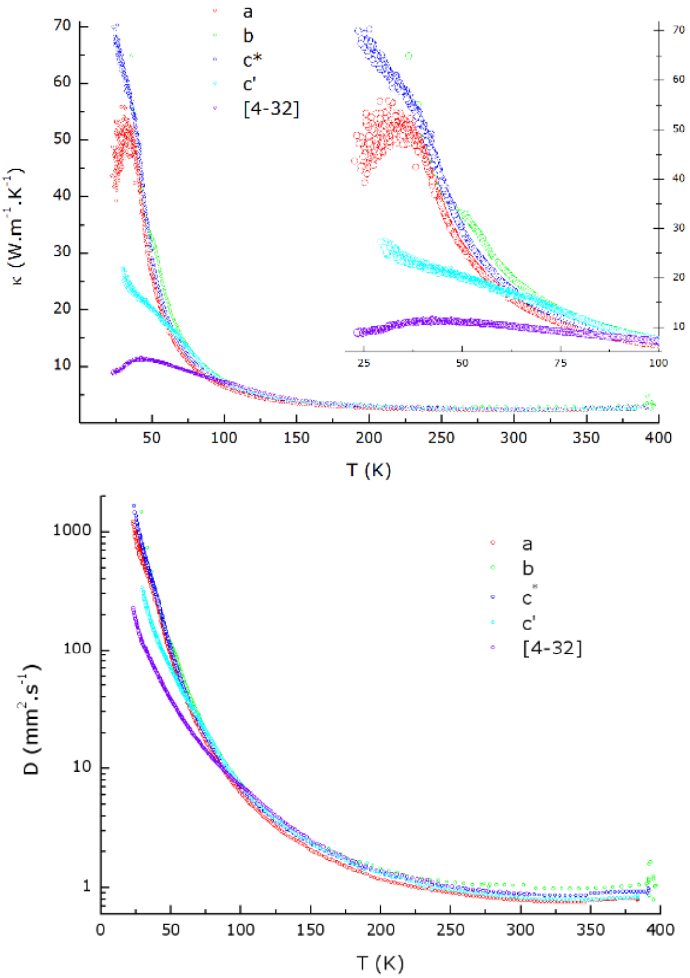

Fig. 5. Top: thermal conductivity of LGEB7 measured along the crystallographic directions **a**, **b**, **c***, **c'** and along the growth direction; Bottom: related thermal diffusivity along the same directions.

#214086 - $15.00 USD Received 16 Jun 2014; revised 23 Jul 2014; accepted 24 Jul 2014; published 11 Sep 2014

Table 3. Thermal conductivity (in units $W.m^{-1}.K^{-1}$) of LGEB7 and LEB crystals, compared with those of related crystals, along the crystallographic and principal axes, at 300 K.

	LEB	LGEB7	$Li_6Y(BO_3)_3:Yb^{3+}$ [3]	$Li_6Gd(BO_3)_3:Yb^{3+}$ [4]	$Li_6Gd_{0.5}Y_{0.5}(BO_3)_3:Yb^{3+}$ [4]
$\kappa_{11} = \kappa'_{11}$		2.21			
κ_{22}		2.98	2.91	1.60	2.00
$\kappa_{33} = \kappa'_{33}$		2.49			
κ_{31}		0.006			
[4–32]	2.57	2.52			
Arbitrary	2.11				
($\mathbf{c}^*$,κ_{III})		Clockwise 1.22°			
($\mathbf{a}$,κ_I)		Anticlockwise 1.22°			

Table 4. Thermal diffusivity values of LEB, LGEB7 and related crystals at 300 K.

Crystal	D[mm^2/s]						References
	$D_{11} = D'_{11}$	D_{22}	$D_{33} = D'_{33}$	D_{31}	[4–32]	Arbitrary	
LEB					0.90	0.74	This work
LGEB7	0.79	1.07	0.89	0.0013	0.90		This work
($\mathbf{c}^*$, D_{III})	Clockwise 0.74°						
($\mathbf{a}$, D_I)	Anticlockwise 0.74°						
$Li_6Y(BO_3)_3:Yb^{3+}$		1.07					[3]

4.3 Microhardness

Hardness is the resistance offered by a material to localized plastic deformation caused by scratching or indentation. Table 5 reveals the hardness anisotropy according to the orientation of the crystal. If we evaluate the microhardness anisotropy by means of the ratio between the two extreme load dependent microhardness values, we find ~1.7. The maximum value corresponds, on Mohs scale, to ~8, which is close to the quartz hardness. Since the distances between Gd-O and Eu-O are comparable in the LEB and LGB crystals, the force necessary to break these bonds can be looked upon as equal. The microhardness anisotropy in the LGEB crystal has some relationship with the orientation of the polyhedra in the compound. Indeed, the maximum hardness is observed along the [010] and [00-1] directions, which are perpendicular and parallel, respectively, to the (Gd,Eu)-O polyhedra chains. It is remarkable that the anisotropy trend in LGEB7 crystals is the same in the microhardness, thermal conductivity and thermal expansion measurements. The highest values are obtained along the **b** direction which is the direction in which the distance between (Eu^{3+},Gd^{3+}) cations is the highest. The higher microhardness found in LGEB7 crystal, with respect to LEB crystal, is likely to be due to the cristallochemical disorder introduced by the Gd^{3+} cations. The order of magnitude found, ~10 GPa, also suggests that the elastic strain energy introduced by the Eu^{3+} cations substitution for Gd^{3+} cations should remain negligible, which is consistent with the value of the depletion coefficient established in section 2.

Table 5. Load-dependent Knoop microhardness along the crystallographic directions.

Crystal	Orientation	Average Knoop hardness (HK0.025)	Mohs-hardness
$Li_6Gd_{0.25}Eu_{0.75}(BO_3)_3$	[-100]	715,2 (7 GPa)	~6.5
	[010]	1225,8 (12 GPa)	~8
	[00-1]	936 (9.2 GPa)	~7.4
	[4–32]	936,4 (9.2 GPa)	~7.4
$^6Li_6Eu(^{10}BO_3)_3$	[4–32]	603,6 (5.9 GPa)	~6.3
	Arbitrary	622,2 (6.1 GPa)	~6.3
$Li_6Gd(BO_3)_3:Yb^{3+}$	Arbitrary	430 (4.2 GPa) [4]	~4-5
$LiGd_6O(BO_3)_3:Yb^{3+}$	Arbitrary	930 (9.1 GPa) [34]	~7.4

#214086 - $15.00 USD Received 16 Jun 2014; revised 23 Jul 2014; accepted 24 Jul 2014; published 11 Sep 2014

5. Spectroscopic properties

5.1 Polarized Raman spectroscopy

Raman spectra of oriented LEB and LGEB7 single crystals have been carried out, to get informations about the symmetry properties of the normal vibration modes and also to give the highest phonon frequencies and density of states. These aspects are useful to estimate the multiphonon emission non radiative decays probabilities or to assign phonon sidebands. Raman spectra at room temperature with a 2 cm^{-1} resolution of the as-grown LEB and LGEB crystals between 200 cm^{-1} (50 μm) and 1600 cm^{-1} (6.25 μm) were recorded with an HORIBA (JOBIN YVON) Raman spectrometer using the 752 nm radiation of an Ar-Kr laser for excitation. A Notch filter was used for the rejection of the Rayleigh light. The polarization study is performed parallel and perpendicular to the C_2 axis. The internal vibrations of the $(BO_3)^{3-}$ group are considered first. The vibrational spectrum of the isolated $(BO_3)^{3-}$ group (with a D_{3h} symmetry) presents six internal vibrational degrees of freedom, which gives rise to four bands: the Raman active symmetric stretch $\upsilon_1(A_1')$ around 940 cm^{-1}, the infrared active out-of plane bend $\upsilon_2(A_2'')$ around 740 cm^{-1}, the asymmetric stretch $\upsilon_3(E')$ around 1330 cm^{-1} and the in-plane bend $\upsilon_4(E')$ around 610 cm^{-1}, these last two vibration modes being doubly degenerated and both Raman and infrared active. The internal vibrational bands seen for the free $(BO_3)^{3-}$ can be perturbed in the crystal. These vibrational bands may be split due to the symmetry of the crystal site and due to interactions with the other $(BO_3)^{3-}$ groups contained in the primitive unit cell. Since the three crystallographically-independent B atoms occupy 4e Wyckoff positions (general positions), the point symmetry of the $(BO_3)^{3-}$ molecular groups is reduced to C_1. Hence, the degeneracy of the υ_3 and υ_4 vibrations is removed according to the scheme: $E' \rightarrow 2A$. The complete correlation diagram for the internal $(BO_3)^{3-}$ vibrations is presented in Table 6. Now, the external modes (lattice vibrations) can be further subdivided into translational and rotational modes coming from the $(BO_3)^{3-}$ groups (each one possesses three translational and three rotational degrees of freedom) and from the three translational degrees of freedom of each cation. All together, this gives a total of 39 A_g + 39 B_g Raman active lattice vibrations. Figure 6 presents the polarized Raman spectra of the samples at RT, for the scattering configurations *Z(XX)-Z Z(YY)-Z, Z(XY)-Z* and *Z(YX)-Z*, and the observed frequencies with their assignments are summarized in Table 7. We assigned the observed Raman wave numbers in the region 500-1500 cm^{-1} to four fundamental modes of vibration of the trigonal $(BO_3)^{3-}$ group corresponding to typical B–O bond vibration modes of borate anions, whereas the low-frequency modes (below 550 cm^{-1}) correspond to external modes of the matrices [35–39].

Table 6. Correlation diagram for LEB and LGEB7 single crystals.

$(BO_3)^{3-}$ molecular group "D_{3h}"	Site group $C_1 \times 3$	Factor group C_{2h}
$\upsilon_1 \rightarrow A_1'(R)$	$A \times 3$	$3 \times (A_g(R) + B_g(R) + A_u(IR) + B_u(IR))$
$\upsilon_2 \rightarrow A_2''(IR)$	$A \times 3$	$3 \times (A_g(R) + B_g(R) + A_u(IR) + B_u(IR))$
$\upsilon_3, \upsilon_4 \rightarrow E'(R, IR)$	$2A \times 3$	$3 \times (2A_g(R) + 2B_g(R) + 2A_u(IR) + 2B_u(IR))$

#214086 - $15.00 USD Received 16 Jun 2014; revised 23 Jul 2014; accepted 24 Jul 2014; published 11 Sep 2014

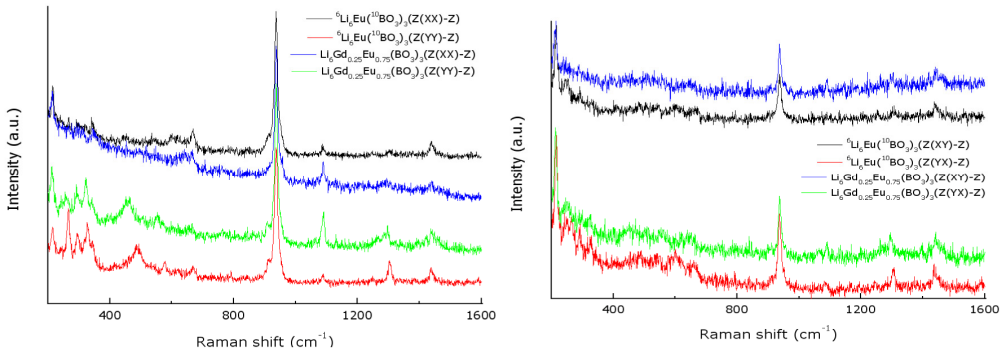

Fig. 6. Polarized Raman spectra of the oriented LEB and LGEB7 single crystals at room temperature.

Table 7. Observed Raman wavenumbers (in cm^{-1}) of LEB and LGEB7 single crystals, and their proposed assignments.

$^6Li_6Eu(^{10}BO_3)_3$				$Li_6Gd_{0.25}Eu_{0.75}(BO_3)_3$				Assignments
Z(XX)-Z(A_g)	Z(YY)-Z(A_g)	Z(XY)-Z(B_g)	Z(YX)-Z(B_g)	Z(XX)-Z(A_g)	Z(YY)-Z(A_g)	Z(XY)-Z(B_g)	Z(YX)-Z(B_g)	
	266	247	247		255		245	Lattice vibrations
	294	292	292		292	288	299	Lattice vibrations
	326		328		321		325	Lattice vibrations
341	343			342	342			Lattice vibrations
	489		488		460		471	Lattice vibrations
							507	Lattice vibrations
	576	543	540		554		559	$\nu_4(BO_3)_3$
		600	600					$\nu_4(BO_3)_3$
						647	644	$\nu_4(BO_3)_3$
668	668	666	656	667	661			$\nu_4(BO_3)_3$
	791				764			$\nu_2(BO_3)_3$
					909			$\nu_1(BO_3)_3$
913	912							$\nu_1(BO_3)_3$
938 s	938 s	938 s	937 s	938 s	938 s	938 s	937 s	$\nu_1(BO_3)_3$
1087	1089		1082	1088	1090		1092	$\nu_3(BO_3)_3$
		1253		1293	1297	1295	1295	$\nu_3(BO_3)_3$
1306	1304	1307	1306			1304		$\nu_3(BO_3)_3$
1438	1438	1437	1436	1440	1440	1440	1441	$\nu_3(BO_3)_3$

s, strong.

5.2 Polarized absorption spectroscopy

Recently, significant progress was obtained both in the methodological and fundamental description of the anisotropy of the spectroscopic properties in monoclinic crystals [41]. Indeed, linear absorption showed nontrivial behavior, with a strong angular dependence both with the crystal orientation and the polarization direction, but also with the considered

#214086 - $15.00 USD Received 16 Jun 2014; revised 23 Jul 2014; accepted 24 Jul 2014; published 11 Sep 2014

resonant electronic transition of the involved rare earth ions. Such a complete description of the wavelength-dependent anisotropy of absorption is far beyond the scope of this paper. However, we focus here on depicting first insights of such anisotropy.

Firstly, we considered the LGEB7 cube oriented with light propagation along the crystallographic b-axis, which is also parallel to the dielectric *Y*-axis. In this case, the other principal axes (*X*-axis and *Z*-axis) lie in the (**a**,**c**)-plane but are rotated with respect to these crystallographic axes. We selected the strong absorption transition at 393 nm, and we measured the related absorption at room temperature, by rotating the incident linear polarization over 180° around the **b** direction (α-polarization, with the origin from **a***-axis). Figure 7 (left) shows the polarization dependence, fitted with Eq. (2) from [40], showing a modulation between two extreme values for polarizations that correspond to polarization Eigen vectors for a light propagation along the **b**-axis. In this case, these polarization Eigen vectors correspond to the dielectric *X*- and *Z*-axes, typically at 30° and 120° with respect to the **a***-axis, respectively, which is in relatively good agreement with that determined in Section 3.1, as reported in Table 1. We emphasize once more that the dielectric frame partially differs from the crystallographic frame in monoclinic systems, which is intrinsic to monoclinic systems. The maximum and minimum absorption cross sections typically corresponding to 30° and 120°, are 6×10^{-21} cm^2 and 5.14×10^{-21} cm^2 at 393 nm, respectively. These values are larger than those of $Y_{1.866}Eu_{0.134}O_3$ (2.5×10^{-21} cm^2) and of Eu:LYB [2], and less than that of LEB [7].

Secondly, since the polarization dependence has just been discussed above, we have performed the spectral distribution of the absorption for polarizations along the dielectric *X*- and *Z*-axes for the propagation along the **b**-axis, respectively labeled here the σ-polarization and the π- polarization. Figure 7 (right) shows the significant wavelength dependence of the absorption anisotropy, since different electronic transitions show different behavior with respect to the two selected polarizations, similarly to that reported in [41].

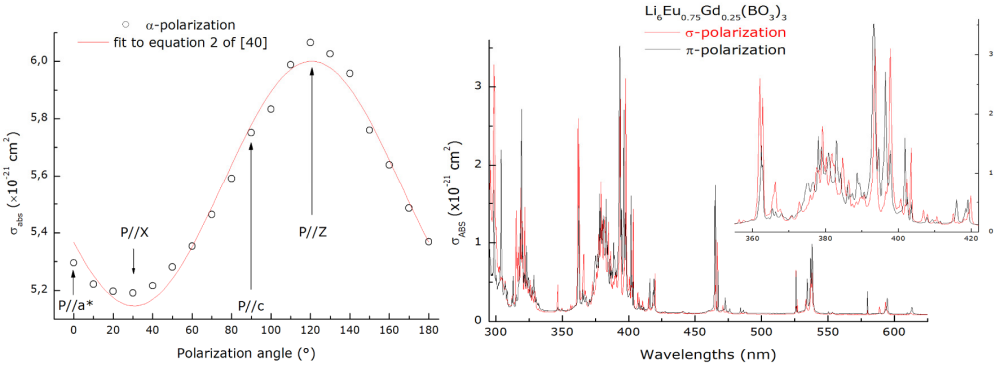

Fig. 7. Propagation along the **b**-axis in polarized light. Left: absorption cross section in the LGEB7 crystal at 393 nm, as a function of polarization orientation; Right: absorption cross section in LGEB7 single crystal in orthogonal Eigen polarizations at RT. The inset is a zoom in the 355-422 nm spectral range, showing the significant wavelength dependence of the absorption anisotropy.

5.3 Polarized emission spectroscopy and Judd-Ofelt analysis

As for the absorption anisotropy, methodological and fundamental descriptions (given in [41]) of the anisotropy of the spectroscopic properties in monoclinic crystals should apply, which is also far beyond the scope of this paper. Due to its $^7F_1$-$^5D_0$ pure magnetic dipole transitions from the ground state and the absence of degeneracy of the $^7F_0$ ground state and of the $^5D_0$ excited state, Eu^{3+} cations stand as the most significant luminescent probe to investigate their crystal-field symmetry in the lattice [10]. Furthermore, they may provide informations on crystal structure, order-disorder issues [11] and different chemical bonds in solids. Emission

#214086 - $15.00 USD Received 16 Jun 2014; revised 23 Jul 2014; accepted 24 Jul 2014; published 11 Sep 2014

cross-section and fluorescence lifetime stand among the most important parameters for the assessment of laser potential of a crystal. A norm has risen that consists of estimating these properties using intensity parameters Ω_λ ($\lambda = 2,4$) based on the Judd–Ofelt theory as discussed by Malta *et al*. [42]. The Judd–Ofelt (JO) parameters contain odd crystal field terms, radial integrals and perturbation energy denominators which are related to local structure and chemical bonding surrounding the optically active rare-earth ions in the crystal. However, some transitions in Eu^{3+} ions challenge the standard JO theory, because they violate selection rules such as forbidden $^5D_0$-$^7F_0$. Some of these transitions are primarily magnetic dipole in nature, but do occur as electric dipole transitions with low intensity in some materials. J-mixing, electronic correlations, dynamic coupling and Wybourne-Downer mechanism [43] are essential mechanisms that have been put forward to explain shortcomings of standard JO theory.

Furthermore, the crystal structure of $Li_6Eu_{1-x}Gd_x(BO_3)_3$ is monoclinic, which can provide further degrees of freedom for the polarization rotations. In this case, the crystallographic principal thermal and optical axes differ. Hence, it is not surprising that our thermo-mechanical and spectroscopic properties revealed a strong anisotropic biaxiality effect. The room temperature polarized emission spectra, calibrated in cross-section units by the Fuchtbauer–Ladenburg (FL) method, of the LGEB6 and LGEB7 crystals, after excitation in the $^5L_6$ (393 nm) levels, is shown in Fig. 8. JO intensity parameters Ω_J ($J = 2,4,6$) are crucial for evaluating the performance of the laser and luminescent materials, and well known for describing the effect of local structure and bonding states in the vicinity of the rare earth cations. Owing to the particular features of the reduced spin-orbit and coulombic repulsion matrix elements of the Eu^{3+} 4f electronic configuration, the Judd–Ofelt parameters can be obtained by using the emission spectra data. We evaluated the JO intensity parameters using the ratio of the integrated intensity of the $^5D_0 \rightarrow {}^7F_{2,4,6}$ electric dipole transitions, $\int I_J(\nu)d\nu$, to the integrated intensity of the $^5D_0 \rightarrow {}^7F_1$ purely magnetic dipole transition, $\int I_1(\nu)d\nu$, according to [44]. The Judd-Ofelt formalism that we adopted is given in [45]. The JO parameters, oscillator strengths, spontaneous emission probabilities, branching ratios, the ratio of integrated emission intensity of the hypersensitive transition $^5D_0 \rightarrow {}^7F_2$ to that of the $^5D_0 \rightarrow {}^7F_1$ magnetic transition, R, the radiative lifetime and the quantum efficiency are gathered in Table 9. The emission band for the $^5D_0$-$^7F_6$ transition, centered around 810 nm, could not be measured accurately because of limitations of our detector in this spectral range. We found that $\Omega_2 > \Omega_4$ for both LGEB6 and LGEB7 crystals, except in σ-polarization for LGEB7 where $\Omega_2 \approx \Omega_4$. The radiative probability of the $^5D_0 \rightarrow {}^7F_2$ transition depends mainly on the Ω_2 value which confirmed that the $^5D_0 \rightarrow {}^7F_2$ transition is predominant as in LEB crystals [7]. The stimulated emission cross section for a given transition from state J to state J_0 can be evaluated by the Futchbauer-Ladenburg expression given below:

$$\sigma_e = \frac{1}{8\pi c n_p^2} \beta_R^p \frac{1}{\tau_R} \lambda^5 \frac{I_e^p(\lambda)}{\int \lambda I_e^p(\lambda) d\lambda} \tag{10}$$

In this formula, c, n_p, β^p_R, τ_R, λ and I^p_e symbolize the speed of light, the average refractive index for a given polarization, the branching ratio for a given polarization, the radiative lifetime, the wavelength and the polarized emission intensity, respectively. The strongest emission cross-section in σ-polarization is about 1.07×10^{-20} cm^2 at 612.8 nm in LGEB7, which is higher than that obtained in LEB [7] and in Eu^{3+}:LYB (4×10^{-21} cm^2) [2]. However, it remains much smaller than the emission cross section of a $Y_{1.866}Eu_{0.134}O_3$ crystal elaborated by the flux method described in [16], which is $\approx 1.8 \times 10^{-20}$ cm^2 at 610.4 nm. This comparison is quite relevant to us because this crystal was one of the first "historical" crystals to lase in

#214086 - $15.00 USD Received 16 Jun 2014; revised 23 Jul 2014; accepted 24 Jul 2014; published 11 Sep 2014

1963 [13], and the only one known to date that proved laser operation based on Eu^{3+} cations. Nevertheless, it is noticeable that the dissolution of the Gd^{3+} cations in the LEB compound substantially improves the emission cross-section. It should be noted too that the LGEB7 emission cross section is relatively higher than that of the LGEB6 in σ-polarization (9×10^{-21} cm^2 at 613.6 nm). The $^5D_0 \rightarrow {}^7F_1$ emission spectra are much more simple than that found at 77 K in Eu^{3+}:LYB powder sample [57]. The $^7F_1$ multiplet crystal field splitting in the three crystals, ≈172 cm^{-1} in the three borate crystals investigated here, is ~0.46 times the energy difference between the $^7F_1$ barycenter and the ground state $^7F_0$, and the overall crystal field splitting of the ^7F_J (J = 2-4) are relatively small, which leads to the obvious conclusion that B^4_q and B^6_q parameters are small and so energy transfers towards impurities in the EuO_8-based chains should be hindered. With the $^7F_1$ energy sublevels structure which our data unveil, we can estimate the B^2_0 and B^2_2 crystal field parameters according to the formula given in [46]. These parameters were found to be $B^2_0 = -606$ cm^{-1} and $B^2_2 = -48$, -49 and -78 cm^{-1} in LEB, LGEB6 and LGEB7 crystals, respectively.

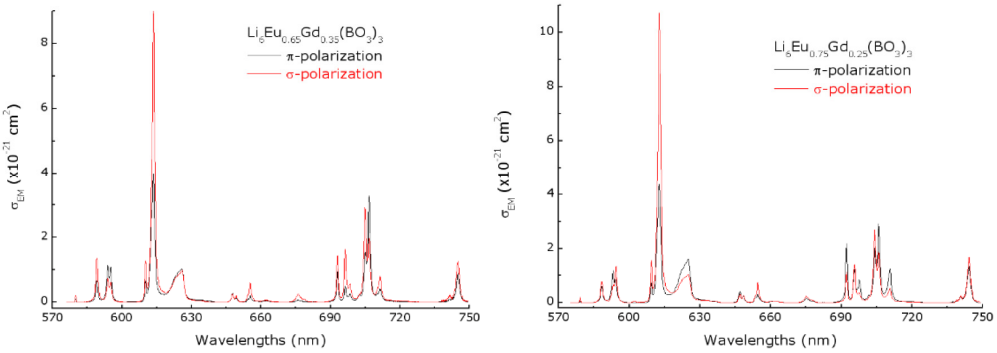

Fig. 8. FL-calibrated stimulated emission cross-section of the LGEB6 and LGEB7 single crystals in polarized direction at room temperature.

5.4 Judd-Ofelt and crystal field parameters calculations

π- or σ-polarization effects on the LEB absorption spectra were established in [7]. They are difficult to analyze because the crystal is biaxial, and also because the Eu^{3+} ground state in this crystal is not a pure $^7F_0$, but a mixture of $^7F_0$, $^7F_2$ (crystal field), $^5D_{1,\mu=0}$, $^5D_{2,\mu=0}$, $^5D_{3,\mu=0}$ (spin-orbit) states, which introduces some deviation from the only selection rule which takes into account the polarization index. This is remarkably illustrated by our measurements. Strictly speaking, in π-polarization, the 3j-symbol rule is $|\Delta M_J(\pi)| = 0,2,4,6$, and in σ-polarization, it reads $|\Delta M_J(\sigma)| = 1,3,5,7$. For example, in spite of the fact that the $^7F_0 \rightarrow {}^5D_0$ and $^5D_0 \rightarrow {}^7F_0$ transitions are forbidden from all viewpoints, we do observe them in both polarized absorption and emission spectra of the three crystals investigated here. The stronger intensity in σ-polarization than in π-polarization in both absorption and emission spectra suggests that the contribution of the $^5D_1$ spin-orbit multiplet to the ground state wavefunction is higher than that of the $^7F_2$, consistently with the relative magnitude of the spin orbit coupling constant and the crystal field strength. Indeed, it was found in EuF_3, where Eu^{3+} ions adopt a C_s point symmetry and their $4f^6$ electronic configuration displays spin orbit multiplets splitting very similar to that encountered in LEB, that the $^7F_0$ wavefunction contains 3.5% of $^5D_{1,\mu=0}$ and 2.8% of $^5D_{3,\mu=0}$ states, among other ones, and the $^7F_1$ wavefunction contains 2.9% of $^5D_{1,\mu=\pm1}$, 0.01% of $^5D_{2,\mu=\pm1}$ and 2.2% of $^5D_{3,\mu=\pm1}$, among other states [58]. The $^7F_2$ state contribution might be estimated from the ratio of $^5D_0 \rightarrow {}^7F_2$ and $^5D_0 \rightarrow {}^7F_0$ emission cross sections in π-polarization, and be in the range ~1.9(LEB)-3.8(LGEB7)%. Another interesting case is the $^7F_1 \rightarrow {}^5D_0$ absorption band, which is a pure magnetic dipole-assisted transition. The absorption band in LEB crystals at 589 nm in π-polarization completely vanishes in σ-

#214086 - $15.00 USD Received 16 Jun 2014; revised 23 Jul 2014; accepted 24 Jul 2014; published 11 Sep 2014

polarization [7]. Consequently, this level ($M_J = 0 \rightarrow M_{J'} = 0$) can be assigned the crystal quantum number 0. Then, at 593.5 and 594.9 nm we observe the two crystal-field sublevels $M_J = \pm 1$, virtually degenerated [7]. If J was a pure 0, we should not observe these transitions in π-polarization. In the polarized emission spectra of Fig. 8, even if the σ-polarization is not relevant in a biaxial crystal, the fact that many bands are not completely extinguished in one polarization or another can be taken as indication of the ground state multi-J mixture. The emission spectra show the $^5D_0$-^7F_J ($0 \rightarrow J$, J = 0 to 4) transitions. The single forbidden $J = 0 \rightarrow J' = 0$ line is a new evidence for the existence of one single luminescent site, already proved by the X-ray crystal structure determination. The $^5D_0 \rightarrow {}^7F_1$ transition exhibits one narrow line around 588-589 nm and two other lines very close to each other (slightly split doublet) between 593 and 596 nm. The $^5D_0 \rightarrow {}^7F_2$ transition displays one narrow line at 609-610 nm and two other quite broad peaks, corresponding to one doublet, around 611-613 nm, and a set of vibronic lines around 622-626 nm, respectively [57]. The $^5D_0 \rightarrow {}^7F_4$ transition exhibits seven lines over nine expected, one line clearly lorentzian (around 692 nm) and three slightly split doublets (around 695-698 nm, 704-707 nm and 709-711 nm). One additional line is seen in π-polarization around 701-702 nm. If this sequence of slightly split doublets would be complete, it could be understood as a slightly distorted high symmetry site of the Eu^{3+} ion and one could assign them, by comparing with the yttrium site in the $LiYF_4$ crystal, a D_{2d} or S_4 point group symmetry [46–48]. In our case, the situation is not that clear, and a D_2 point symmetry at best can be put forward (*vide infra*). To progress towards crystal field parameters determination, the simple overlap model (SOM) [49] and the method of equivalent nearest neighbours (MENN) [50] were applied, together with the Auzel-Malta expression (ΔE_{theo}) [51], to calculate the crystal field parameters (CFP) and predict the $^7F_1$ sublevel positions and splitting. The reason for such a procedure is that the SOM and ΔE_{theo} have reproduced such quantities in many systems very satisfactorily throughout the years. To perform calculations one needs the spherical coordinates of the nearest neighbours (NN), the Eu^{3+} ion at the origin, and the maximum overlap ($\rho_0 = 0.05$) between the 4f and 2p orbitals [52]. Here it is important to comment that only the NN are used because the local symmetry defines the number of crystal field levels [46]. The structure of peaks assigned to the $^7F_1 \rightarrow {}^5D_0$ and $^5D_0 \rightarrow {}^7F_1$ transitions leads to the suggestion that the ground state of the $^7F_1$ manifold is non-degenerate ($\mu_J = 0$). Thus, B^2_0 must be negative. The closeness of the other two lines indicates that the B^2_2 parameter is of small magnitude, as it has been obtained from the emission spectra. A high R-value, evoked in section 5.3, is generally interpreted in terms of high asymmetry of the EuO_8 polyhedra. Indeed, the continuous symmetry analysis performed in LEB crystals [7] revealed that the deviation from the ideal symmetry is important: 11.6% from the mirror plane (C_s point group) and 28.2% from the twofold symmetry axis (C_2 point group), resulting in a strongly distorted gyrobifastigium polyhedron EuO_8. So C_s, C_2, C_{2h} or C_{2v}, but above all, D_2 are the closest point groups that can be conceived, as we will discuss now based on Eu^{3+} cations local structure drawings of Fig. 9. Since we observe two of the $^7F_0 \rightarrow {}^5D_1$ absorption peaks and five of the $^7F_0 \rightarrow {}^5D_2$ absorption peaks, it is not straightforward with a room temperature spectrum to apply the general symmetry descent scheme given in [47]. However, it is possible to use the emission general scheme of [46] and conclude that in the three crystals LEB, LGEB6 and LGEB7 a C_{2v} point symmetry can be put forward.

#214086 - $15.00 USD Received 16 Jun 2014; revised 23 Jul 2014; accepted 24 Jul 2014; published 11 Sep 2014

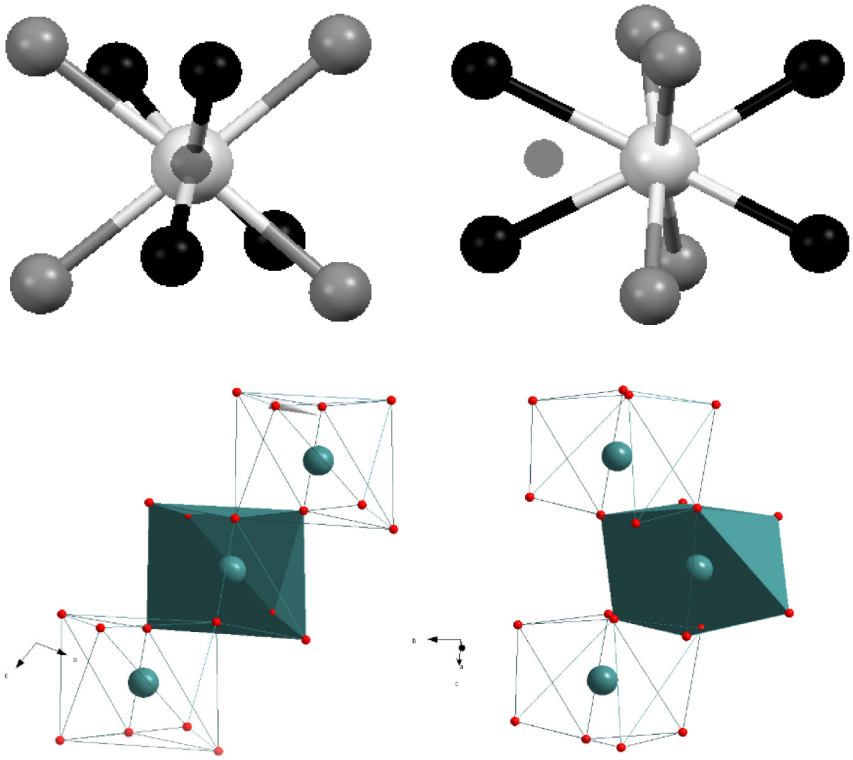

Fig. 9. EuO_8 polyhedra and their orientation. Left: the sheet plane is (**a**,**c**) and **b** is perpendicular to the sheet; Right: the same figure rotated by 90° resulting in **b** belonging to the sheet plane and the (**a**,**c**)-plane perpendicular to the sheet. π-polarization means (**P**) parallel to **b**, and σ-polarization means either (**P**) perpendicular to **b** in the sheet plane or (**P**) perpendicular to both **b** and the sheet plane.

The LEB single crystal XRD data published in [7] gives average atomic positions, and it was found from the Fourier analysis of the electronic density that there is some 4% of Eu vacancies, which implies cristallochemical disorder likely to induce a slight distribution of crystal field around Eu^{3+} cations. This XRD characterization was done with the aim of getting an estimate of the Eu concentration, which was made possible by two facts: the first one is the unusually high number of collected diffraction spots, and the second one is, in this compound, the much higher Z of Eu atoms compared with any other element of the structure, and so the diffusion contrast with Li, B and O elements which proved to be outstanding. In Fig. 9, the four dark grey balls are the oxygen ions lying approximately on the (**a**,**c**)-plane. One can note the centroid (small ball in gray) indicating a z axis parallel to the **b** axis (with the maximum moment of inertia) perpendicular and out of the sheet, thus the principal axis of symmetry. The imaginary x axis horizontal and in the sheet plane in Fig. 9 left, and perpendicular to the sheet plane in Fig. 9 right, is close to the [71-4] direction. By applying a C_2 operation around both these fictitious z and x axes, one can note that each black-oxygen ion goes very approximately to the position of any other black-oxygen ion. Thus, all black-oxygen ions are almost equivalent to each other. Under the same operations, this is also true for the four gray-oxygen ions. This is to show that, by symmetry, as required in the first premise of the MENN, one has only two different charge factors, then only two degrees of freedom, to predict the $^7F_1$ energy sublevel positions and splitting using non-parametric crystal field models [53]. Table 8 shows the calculated quantities. In red are the experimental sublevels and the intensity parameters for π-polarization.

#214086 - $15.00 USD Received 16 Jun 2014; revised 23 Jul 2014; accepted 24 Jul 2014; published 11 Sep 2014

Table 8. Charge factors (g), polarizabilities (α, in 10^{-24} cm^3), $^7F_1$ energy sublevels and splitting and crystal field parameters (in cm^{-1}) and intensity parameters (Ω_λ, in 10^{-20} cm^2). In red are experimental data and the set of α which has reproduced the experimental Ω_λ. (*) average values.

g_1	g_2	$E_{calc}(E_{exp})$	μ_J
0.498 ($R_<$)	0.252 ($R_>$)	276 (268)	0
B^2_0	–488	349 (405)	–1
B^2_1	56	490 (442)	+ 1
B^2_2	–157	ΔE	ΔE_{theo}
		214(174)	174
α_1	α_2	α_1 (π)	α_2 (π)
1.052	2.432	0.630	2.532
Ω_2	Ω_4	Ω_2	Ω_4
6.0(*)	1.6(*)	7.52	1.55

The negative B^2_0 signal confirms that the $\mu_J = 0$ sublevel is really the ground state of the $^7F_1$ multiplet. The small magnitude of the B^2_1 parameter is an indication that the local structure of the luminescent ion is close to a high symmetry site, namely, C_{2v} or D_{2d}. However, the quite strong magnitude of the B^2_2 parameter does not predict a so slightly split $M_J = \pm 1$ doublet. This has already been encountered elsewhere [48] and the interpretation is being discussed in our group. The emission spectra, however, shows the $M_J = \pm 1$ doublet split is ≈37 cm^{-1} in LEB, and ≈34 cm^{-1} in both LGEB6 and LGEB7 crystals. The Ω_λ-parameters have been satisfactorily reproduced for the LGEB7 sample by comparing with the π-polarization measurements, as well as for an average of all intensity parameters, with physically acceptable values of polarizabilities (Table 8). Further, the polarizability of the closer NN ions was smaller than that of the farther NN ions. This is expected because closer ions have bonds stronger than the farther ions have. This has been observed even for the average Ω_λ. The local symmetry of the luminescent ion in the LGEB6 sample is not different from that of the LGEB7 sample. Thus, the differences in the magnitude of the Ω_λ-parameters when π-polarizations are compared are directly related to the selection rules governed by the irreducible representations of the initial and final state of each transition. To deepen this analysis further a precise knowledge of the ground state wave function is needed.

5.5 Fluorescence decays

The luminescence decays of the $^5D_0 \rightarrow {}^7F_2$ transition in LEB, LGEB7 and LGEB6 crystals have been measured at 300 K. For two reasons these compounds seemed to be interesting hosts for studying migration among Eu^{3+} ions: (a) since their crystal structure contains only one crystallographically nonequivalent Eu^{3+} site, with a point group symmetry that lifts the J = 0→J' = 0 extinction rule, the multipolar processes increase as the oscillator strength of the $^7F_0 \rightarrow {}^5D_0$ transition increases; (b) the short Eu-Eu distances along **c** (3.9 Å), which makes at low temperatures the transfer occur by exchange [54]. The Eu-Eu distances between the chains are ≈7.2 Å along **a** and ≈8.5 Å along **b**. As was shown in [12], the luminescence output of the Eu^{3+} cations in the $Li_6Gd_{1-x}Eu_x(BO_3)_3$ solid solution increases with x until x = 0.85 and is barely affected by temperature between 90 and 300 K, which indicates that above this concentration the excitation energy can migrate over the Eu^{3+} sublattice and get trapped at quenching impurities sites. Indeed, the absence of intermediate levels between the $^5D_0$ spin-orbit multiplet and the $^7F_0$ ground state in the Eu^{3+} cations energy level diagram excludes that these levels could be depopulated by cross relaxation processes responsible for the concentration quenching occurring in the majority of the other rare earth cations. For multipolar coupling, the probability of energy transfer depends on the probability of the multipolar transitions on the ions involved. For Eu^{3+} at low temperatures the only resonant transition giving rise to energy transfer is $^5D_0 \rightarrow {}^7F_0$. This transition is strongly forbidden,

#214086 - $15.00 USD Received 16 Jun 2014; revised 23 Jul 2014; accepted 24 Jul 2014; published 11 Sep 2014

which makes energy transfers at low temperatures very improbable (the typical peak cross section values in LEB, LGEB6 and LGEB7 crystals are ~2 × 10^{-22} cm^2 in σ-polarization). As temperature increases, higher-lying ^7F_J levels are thermally populated and additional resonant transition pairs ($^5D_0 \rightarrow {}^7F_1$ and $^5D_0 \rightarrow {}^7F_2$) become possible. As shown on Fig. 10, the fluorescence decays display a non-exponential behavior, thus implying that there exists an energy transfer between Eu^{3+} ions, and/or from Eu^{3+} ions to other luminescent centers. If the donor and acceptor ions are randomly distributed in the host and the migration processes are negligible in comparison with donor–acceptor energy transfers, the time evolution of the donor population after pulsed excitation, is given by the well-known Inokuti–Hirayama model [55]. On the other hand, if migration processes among donors are dominant, then the problem is more complex and different approximations have been developed to handle this case theoretically. One possibility is to consider the energy migration as a diffusion process. This method was adopted by Yokota and Tanimoto [56], who obtained a simple expression for the time evolution of excited donors. Another situation is the case where energy migration occurs on a one–dimensional system of donor sites, with randomly distributed acceptors of infinite trap depth, for which Movaghar *et al.* [54] derived an expression for the rise of donor luminescence intensity at long times:

$$I(t) = I_0 \exp(-t/\tau_0 - Bt^{1/3}) \tag{11}$$

with $B = 3\left(\frac{1}{4}\pi^2 C_a^2 P\right)^{1/3}$, τ_0 the radiative decay time, C_a the acceptor concentration and P the donor-donor transfer probability. The $^5D_0$ radiative lifetime was determined to be 1.9 and 2.2 ms at 300 K in LGEB7 and LGEB6 crystals, respectively (Table 9). The internal quantum efficiency η for the $^5D_0$ level is defined as the ratio of the number of photons emitted by the number of photons absorbed which can be calculated using the fluorescent and radiative lifetimes, $\eta = \frac{\tau_f}{\tau_R}$. The values for the $^5D_0$ level are found to be 92.6% for the LGEB7 and 93.2% for LGEB6, which stresses the weak effect of non-radiative processes such as multiphonon emission and cross-relaxation mechanisms.

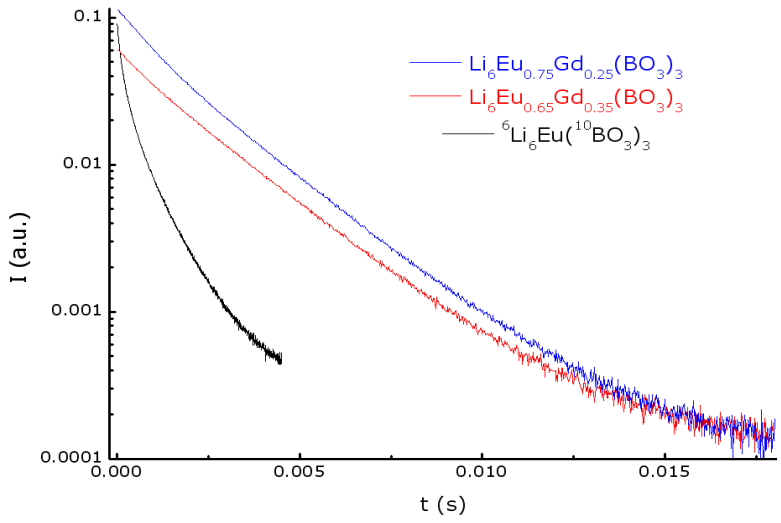

Fig. 10. Fluorescence decays measured in the three crystals, LGEB6, LGEB7 and LEB.

#214086 - $15.00 USD Received 16 Jun 2014; revised 23 Jul 2014; accepted 24 Jul 2014; published 11 Sep 2014

Table 9. Results of the Judd-Ofelt analysis in polarized directions carried out in the LGEB7 and LGEB6 single crystals: $\Omega_{2,4}$ JO parameters, electric and magnetic oscillator strength (f), radiative transition rates (A_R), branching ratios (β_R), radiative lifetimes (τ_R) and quantum efficiency (η).

Crystals	Transitions	$\bar{\nu}(cm^{-1})$	Ω_2(× 10^{-20}cm^2)	Ω_4(× 10^{-20}cm^2)	f × 10^{-6}	A_R (s^{-1})	β_R(%)	R	τ_R (ms)	η (%)
$Li_6Gd_{0.25}Eu_{0.75}(BO_3)_3$ $\sigma_{//}$	$^5D_0\rightarrow{}^7F_0$	17266.98	7.36	7.56	0.0016	0.80	0.17	4.50	1.9	
	$\rightarrow{}^7F_1$	16887.33			0.12	59.36	12.24			
	$\rightarrow{}^7F_2$	16187.00			0.60	267.15	55.09			
	$\rightarrow{}^7F_3$	15331.07			0.05	20.09	4.14			
	$\rightarrow{}^7F_4$	14260.05			0.38	134.80	27.80			
	$\rightarrow{}^7F_5$	13449.72			0.009	2.76	0.57			
$Li_6Gd_{0.25}Eu_{0.75}(BO_3)_3$ $\sigma_{\perp}$	$\rightarrow{}^7F_0$	17266.39	10.32	5.84	0.0038	1.94	0.34	6.37		92.6
	$\rightarrow{}^7F_1$	16890.32			0.12	59.39	10.41			
	$\rightarrow{}^7F_2$	16253.55			0.84	379.00	66.42			
	$\rightarrow{}^7F_3$	15309.55			0.060	24.14	4.23			
	$\rightarrow{}^7F_4$	14277.33			0.30	104.57	18.32			
	$\rightarrow{}^7F_5$	13445.74			0.005	1.59	0.27			
$Li_6Gd_{0.35}Eu_{0.65}(BO_3)_3$ $\sigma_{//}$	$\rightarrow{}^7F_0$	17242.27	5.88	4.87	0.0018	0.94	0.25	3.60	2.23	93.2
	$\rightarrow{}^7F_1$	16863.41			0.12	59.10	15.80			
	$\rightarrow{}^7F_2$	16188.56			0.48	213.28	57.01			
	$\rightarrow{}^7F_3$	15310.28			0.03	12.29	3.28			
	$\rightarrow{}^7F_4$	14213.06			0.25	85.96	23.00			
	$\rightarrow{}^7F_5$	13431.29			0.008	2.49	0.66			
$Li_6Gd_{0.35}Eu_{0.65}(BO_3)_3$ $\sigma_{\perp}$	$\rightarrow{}^7F_0$	17241.88	8.64	6.82	0.0039	1.98	0.38	5.30		
	$\rightarrow{}^7F_1$	16904.60			0.12	59.54	11.43			
	$\rightarrow{}^7F_2$	16231.68			0.70	315.96	60.70			
	$\rightarrow{}^7F_3$	15289.87			0.049	19.69	3.78			
	$\rightarrow{}^7F_4$	14258.85			0.35	121.58	23.35			
	$\rightarrow{}^7F_5$	13435.26			0.006	1.83	0.35			

Continuous function decay multisite analysis was performed with 50 exponentials fitted to the nonexponential luminescence decays of the LEB, LGEB6 and LGEB7 crystals at 612.8 nm ($^5D_0\rightarrow{}^7F_2$), shown in Fig. 10. The deviation from exponential shape increases from LGEB7 to LEB and it clearly appears on the fits results: while in LGEB7, two exponentials suffice, in LGEB6, a third one appears and in LEB several short time components, certainly due to fast trapping by impurities or vacancies energy levels, appear. The main components of the decays in LGEB6 and 7 correspond to a lifetime around 2.2 ms and 2.4 ms, respectively. However, given the weight of the short time components, average experimental lifetimes of 1.76 ms and 2.05 ms in LGEB7 and LGEB6 crystals, respectively, seems more appropriate values to estimate the fluorescence quantum yield. Fits to Eq. (11) did not work over time intervals larger than 1 ms in LEB crystals, but for the LGEB6 crystal, a reasonably satisfactory fit was obtained over a time interval $\approx 2.8 \times \tau_R$, with τ_R = 2.37 ms, C_a = 0.00246 and P = 35439 s^{-1}, and for the LGEB7 crystal, a less satisfactory fit was obtained over a time interval $\approx 1.85 \times \tau_R$, with τ_R = 2.14 ms, C_a = 0.00264 and P = 57489 s^{-1}. An exhaustive GDMS

#214086 - $15.00 USD Received 16 Jun 2014; revised 23 Jul 2014; accepted 24 Jul 2014; published 11 Sep 2014

chemical analysis performed on a LEB crystal gives only two possible acceptor impurities in the range of concentration C_a: Na = 0.0019 and Yb = 0.00017. It is remarkable that Nd impurities and several rare-earth elements are kept at a very low level, $C_a<3\ 10^{-5}$, except Gd for which $C_{Gd} = 0.0137$.

6. Conclusions

In this work we have determined the eigenvalues of two tensors describing fundamental properties of LGEB7 and LEB crystals, namely the thermal expansion and the thermal conductivity, as well as the Eu^{3+} absorption and emission cross sections anisotropies. In comparison with other laser crystals, LGEB7 exhibits a relatively low anisotropy of thermal conductivity at room temperature. It was found that the anisotropy observed in these crystals is the same for the thermal expansion, the thermal conductivity and the microhardness. The thermal (κ,C_p), mechanical (HK) and thermo-mechanical (α) properties of these crystals, in addition to a series of fractures induced by the manipulation (cutting, polishing), do not suggest a tremendous potential for laser applications, unless a clever thermo-mechanical management of the crystal under laser operation is designed. Moreover, their maximum peak emission cross section is ~1.68 lower than that of the well-known Y_2O_3:Eu^{3+} single crystal, here $Y_{1.866}Eu_{0.134}O_3$, which is itself a difficult system to pump optically. Concerning HSCB applications, our results suggest that LGEB7 is probably the most promising composition, upon which crystal growth efforts should be paid, because of its overall emission intensity and improved hardness, and the presence in its bulk of high concentrations of ^{6}Li, $^{155/157}$Gd and ^{10}B isotopes. Its thermal expansion being equivalent to that of LEB crystals, one expects a similar Debye temperature to that of the latter crystals (≈873 K [7]), and its thermal conductivity remains quite high, at least down to 20 K. Crystal field and intensity parameters calculations have shown that with only two degrees of freedom, namely, g_1 and g_2 for the crystal field parameters of rank 2, and α_1 and α_2 for the intensity parameters, we could reproduce satisfactorily spectroscopic quantities such as the $^7F_1$ level splitting and sublevels positions and magnitude of the Ω_λ-parameters. This is a strong indication that, at least in the case of crystals, old theories and models can interpret quite well such spectroscopic quantities, with no need of numerical procedures.

#214086 - $15.00 USD Received 16 Jun 2014; revised 23 Jul 2014; accepted 24 Jul 2014; published 11 Sep 2014